# Multi-Point Orientation Control of Discretely-Magnetized Continuum Manipulators

Michiel Richter, Venkatasubramanian Kalpathy Venkiteswaran, and Sarthak Misra

***Abstract*—In the past decade, remote actuation through magnetic fields has been used for position and orientation control of continuum manipulators (CMs) with a single magnet at the distal tip. By leveraging multiple points of actuation along the length of the CM it is possible to achieve increasingly complex shapes, which could be of interest in complex navigation tasks, for example, in minimally invasive surgery. In this study we present an approach for multi-point orientation control of discretely magnetized CMs. The approach is demonstrated with a manipulator that contains two permanent magnets, which are each actuated inside a non-homogeneous magnetic field. We formulate an accurate field model that conforms to Maxwell's equations and apply this to the available actuation system. Furthermore, Cosserat rod theory is used to model the manipulator deformation under external wrenches, and is utilized to numerically compute a Jacobian necessary to calculate the actuation inputs. During experiments, a stereo vision setup is used for manipulator shape feedback. Target orientations are manually provided as input to show independent orientation control of the two permanent magnets. Additionally, simulations with an extended virtual clone of the electromagnetic system are performed to show the capability of achieving more complex manipulator shapes. In both scenarios, it is observed that the algorithm is able to independently control the orientation of two interconnected magnets in a non-uniform magnetic field.**

## I. Introduction

Continuum manipulators (CMs) are continuously deformable elastic structures. Compared to traditional rigid link robots, CMs have infinite degrees of freedom (DOFs) which allows them to deform at any point along their length. This property makes CMs dexterous, enabling them to navigate through constricted spaces and cluttered environments [1]. The challenge lies in steering and navigation of CMs, as actuation at multiple points along the CM also requires actuators at those points. However, actuators attached to the body of the CM increase its size, which is disadvantageous in confined workspaces [2]. Magnetic actuation provides the potential for miniaturization by moving the actuation system outside the confined environment [3].

Magnetized CMs can be discretely or continuously magnetized. Discretely magnetized CMs contain rigid magnetic, and flexible non-magnetic material. The rigid magnetic material can be divided into actively magnetized electromagnets [4], or permanent magnets [5]. Alternatively, continuously magnetized CMs consist of magnetic composite polymers [6]. These can be used to fabricate specialized magnetization profiles for target applications [7, 8]. The magnetized CMs deform due to a magnetic wrench, exerted on their magnetic regions by a magnetic field. A theoretical minimum of seven magnetic degrees of freedom is required for wrench control. However, these systems may suffer from magnet orientation-dependent singularities. By instead providing eight magnetic degrees of freedom such singularities are avoided [9].

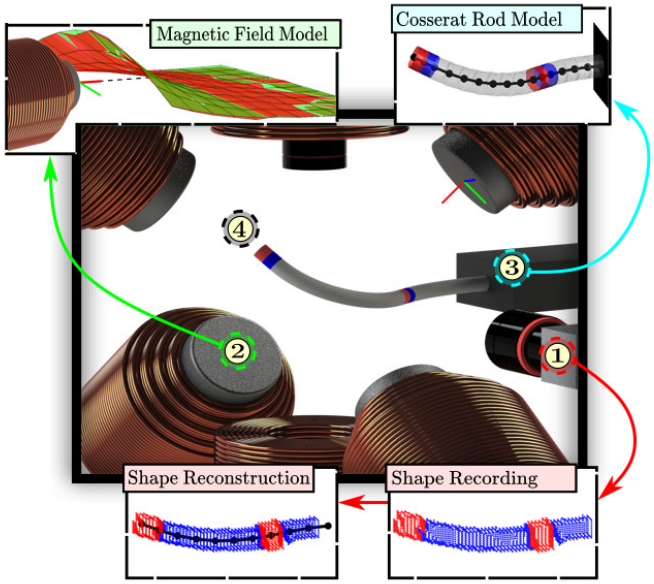


**Fig. 1:** In this study we use BigMag, an array of 6 mobile electromagnetic coils [12], to perform closed-loop orientation control of two permanent magnets carried by a continuum manipulator (CM). ① Shape reconstruction of the CM is performed with a stereo vision setup. ② A model of the magnetic field then predicts exerted magnetic wrenches on the CM. ③ With Cosserat rod theory a quasi-static forward model of the CM is produced. ④ This model is used to predict changes in magnet orientations, due to changes in the currents and positions of the electromagnets, in order to actuate the CM.

In literature, different configurations of magnetic actuation systems have been designed based on application requirements. Such systems employ stationary electromagnets [10, 11], mobile electromagnets [12, 13], or mobile permanent magnets [5], as sources of the magnetic field. The mobile actuation systems have the advantage of an open and typically larger workspace than stationary systems, while requiring smaller external magnets [14]. Precise magnetic field information

This work is supported by the European Research Council (ERC) under the European Union's Horizon 2020 Research and Innovation programme under Grant 866494 project – MAESTRO.

All authors are affiliated with the Surgical Robotics Laboratory, Department of Biomechanical Engineering, University of Twente, 7500 AE Enschede, The Netherlands (e-mail: m.richter@utwente.nl, v.kalpathyvenkiteswaran@utwente.nl, s.misra@utwente.nl).

Sarthak Misra is also affiliated with the Surgical Robotics Laboratory, Department of Biomedical Engineering, University of Groningen and University Medical Centre Groningen, 9713 GZ Groningen, The Netherlands.

from each field source is required for actuation. Previously used approaches model the magnetic field either using an arbitrary function and fit unknown coefficients with least squares optimization [12, 15], or use a first-order dipole approximation [5]. The former approach does not typically enforce constraints on the spatial gradients of the magnetic field, and the latter ignores higher order field effects that are more prominent closer to the field source [16]. A recently used approach, that solves the aforementioned disadvantages, is to express the magnetic field as the gradient of a scalar potential (scalar harmonic function), and use measurement-informed least squares optimization to fit unknown coefficients [17].

A mathematical model of the manipulator is used to compute its deformation under exerted magnetic torques and forces, which result from the interaction with an external magnetic field. These models generally have a trade-off between accuracy and computational efficiency [2, 18]. In our work, Cosserat rod theory is used to model the CM. Cosserat rod theory gives an exact solution to the statics of the CM, while additionally accommodating variations in the stiffness, body loading, and cross-section geometry of a CM [19, 20].

Rigid-link and Cosserat rod models have recently been used for position control of a CM with a single magnet at its distal tip [20, 21]. In addition, unidirectional steering within a uniform magnetic field has been shown with permanent magnets integrated into the distal tip of a CM [22, 23]. Through the actuation of a CM at the distal tip, it is only possible to achieve first-order shapes of the CM body. By introducing multiple actuation points (magnets) along the length of the manipulator, it is possible to achieve higher order shapes, which is of interest in complex navigation tasks during minimally invasive surgery. Compared to existing works, the effect of magnetic forces (field gradients) cannot be neglected when multiple independently controlled magnets are in close proximity. It should be noted that manipulating the field at one magnet inherently changes the field at other magnets carried by the CM. Furthermore, actuation of one magnet inherently actuates the magnets in close proximity. The control algorithm should therefore be able to predict and compensate for this interdependence.

In this study we show closed-loop orientation control of two magnets along a discretely magnetized CM. The magnet orientations are independently controlled by exerting necessary magnetic torques and forces through manipulating the external non-homogeneous magnetic field generated by BigMag, an array of six mobile electromagnetic coils [12]. We formulate a magnetic field model that conforms to Maxwell's equations to accurately predict magnetically exerted wrenches on the CM. A stereo vision setup records the actuation workspace and is used for shape reconstruction of the CM. Cosserat rod theory is applied to construct a forward model of the CM to predict changes in the CM shape due to variations in the external magnetic field. In addition, BigMag is extended with eight additional electromagnets in simulation to improve achievable fields at the workspace edge to show that the control algorithm is able to achieve complex geometries of the CM. All the above-mentioned steps are detailed in the following sections, followed by discussion and conclusions.

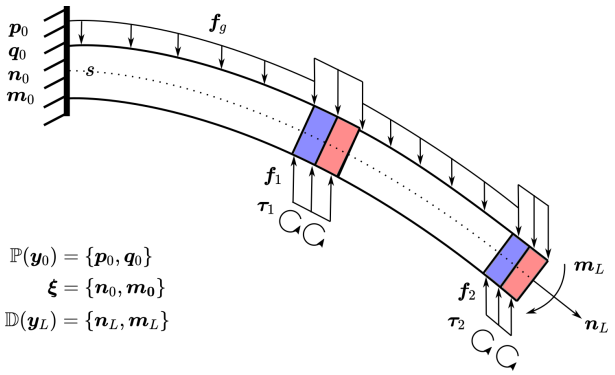


**Fig. 2:** Proximally fixed, and distally free-floating, discretely magnetized continuum manipulator (CM), characterized by a centerline parameter ($s \in [0, L]$), subject to distributed magnetic forces ($\boldsymbol{f}_m(s)$) and torques ($\boldsymbol{\tau}_m(s)$, $m = 1, 2$), and gravitational forces ($\boldsymbol{f}_g(s)$). Material cross-sections along $s$ are characterized by a position ($\boldsymbol{p}(s)$), orientation quaternion ($\boldsymbol{q}(s)$), internal force ($\boldsymbol{n}(s)$), and internal moment ($\boldsymbol{m}(s)$); collected in state parameter vector ($\boldsymbol{y}(s)$). Known proximal and distal boundary conditions are denoted as $\mathbb{P}(\boldsymbol{y}_0)$ and $\mathbb{D}(\boldsymbol{y}_L)$, respectively. Unknown proximal states are collected in an optimization vector ($\boldsymbol{\xi}$).

## II. Theory

In this section, the model used for analyis of the continuum manipulator is described, followed by the formulation of a Cartesian multipole expansion of a scalar potential for accurate, measurement-informed fitting of magnetic field and magnetic field gradient map.

### A. Cosserat Rod Model

Consider a CM attached proximally to a rigid base and free-floating at the distal tip (Fig. 2). The CM carries two permanent magnets: one at an intermediate position along the body and one at the distal tip. The magnets experience a magnetic force and torque within an external magnetic field, causing the CM to deform. Gravity also acts on the CM. To control the shape of a magnetized CM, we need to predict the (change in) shape of the CM when loaded by magnetic forces and torques. For this we use a Cosserat rod model of the CM.

In Cosserat rod theory, the body of the manipulator is characterized by centerline parameter ($s \in [0, L]$), where $L \in \mathbb{R}^+$ represents the manipulator length. Each material cross-section along $s$ is characterized by a material state vector

$$\boldsymbol{y}(s) = \begin{bmatrix} \boldsymbol{p}(s)^T & \boldsymbol{q}(s)^T & \boldsymbol{n}(s)^T & \boldsymbol{m}(s)^T \end{bmatrix}^T, \qquad (1)$$

with $\boldsymbol{p}(s) \in \mathbb{R}^3$ a Cartesian position, $\boldsymbol{q}(s) \in \mathbb{H}$ an orientation (quaternion), $\boldsymbol{n}(s) \in \mathbb{R}^3$ the internal force, and $\boldsymbol{m}(s) \in \mathbb{R}^3$ the internal moment [19, 24]. The evolution of $\boldsymbol{y}(s)$ along $s$ is described by a set of ordinary differential equations that take into account the internal and external loads on the manipulator. The shape of the CM, loaded by magnetic forces and torques and gravity, is then obtained from the manipulator statics, solved as a boundary value problem (BVP) [20].

In Fig. 2, the CM is attached proximally ($s = 0$) to a rigid base and has a proximal boundary condition ($\mathbb{P}(\boldsymbol{y}_0)$);

the free distal tip is in a constant unloaded state and has a distal boundary condition ($\mathbb{D}(\boldsymbol{y}_L)$). We solve the Cosserat rod BVP with forward integration using an explicit Runge-Kutta fourth order method, and convex optimization with Levenberg-Marquardt, with the algorithm adapted from [25] as follows. First, the centerline of the CM is discretized into $N \in \mathbb{N}$ segments; non-uniform discretization is chosen such that transitions from non-magnetic to magnetic material are fully captured. Second, the known proximal boundary condition ($\mathbb{P}(\boldsymbol{y}_0)$), in combination with a guessed optimization vector ($\boldsymbol{\xi}$) of residual unknown proximal parameters, is used to form the proximal material state vector ($\boldsymbol{y}_0$). Third, an explicit Runge-Kutta fourth order method is used for forward integration of $\boldsymbol{y}_0$ to $\boldsymbol{y}_N$. Finally, the residual between distal boundary condition ($\mathbb{D}(\boldsymbol{y}_L)$) and integrated distal states ($\mathbb{D}(\boldsymbol{y}_N)$) is used to update the optimization vector ($\boldsymbol{\xi}$) with convex optimization using Levenberg-Marquardt. If the norm of the residual is below an arbitrarily chosen error threshold, the solution of $\boldsymbol{\xi}$ is accepted and the collection of material state vectors ($\boldsymbol{y}_n$, $\forall n \in \{0, 1, \ldots, N\}$), represents the manipulator shape,

$$\boldsymbol{Y}(\boldsymbol{\xi}) = \begin{bmatrix} \boldsymbol{y}_0 & \boldsymbol{y}_1 & \ldots & \boldsymbol{y}_N \end{bmatrix} \in \mathbb{R}^{13\times(N+1)}, \tag{2}$$

which we call the shape solution.

### B. Magnetic Field Map

The magnetic wrench experienced by the CM (Fig. 2) depends on the external magnetic field generated by the magnetic actuation system. Accurate estimation of magnetic forces and torques follows from the quality of the model that describes the actuation magnetic field. Each actuator magnet represents a source of a magnetic field ($\boldsymbol{B}(\boldsymbol{p}, I) \in \mathbb{R}^3$) with associated spatial field gradients ($\boldsymbol{B}_\nabla(\boldsymbol{p}, I) \in \mathbb{R}^{3\times3}$), where $I \in \mathbb{R}$ denotes the current through an electromagnet. For electromagnets operating outside their saturation region, i.e. where their generated field is linear with current, a unit-current field ($\boldsymbol{\beta}(\boldsymbol{p}) \in \mathbb{R}^3$) and gradient ($\boldsymbol{\beta}_\nabla(\boldsymbol{p}) \in \mathbb{R}^{3\times3}$) model can be formulated and used to linearly describe the field at different operating currents. In the paragraphs below we present a model for the magnetic field that conforms to Maxwell's equations and that can be applied to individual azimuthally symmetric field sources (e.g. solenoids).

In a current-free workspace, the field is both divergence- and curl-free, which allows expressing the field as the gradient of a scalar potential,

$$\boldsymbol{B}(\boldsymbol{p}, I) = \nabla\Psi(\boldsymbol{p}) \cdot I, \tag{3}$$

where $\Psi(\boldsymbol{p})$ is a nonlinear scalar function in the position vector $\boldsymbol{p}$ [26]. Consider an orthonormal body coordinate frame attached to the face of an azimuthally symmetric electromagnet, where $\hat{\boldsymbol{x}}$ is the zenith direction of the electromagnet. Then it can be shown that it is possible to describe the generated magnetic field with a scalar potential given by

$$\Psi(\boldsymbol{p}) = \sum_{k=1}^{P} \Psi_k(\boldsymbol{p}) \cdot a_k, \qquad \Psi_k(\boldsymbol{p}) = \frac{\partial^k}{\partial x^k}\left(\frac{1}{\|\boldsymbol{p}\|}\right), \tag{4}$$

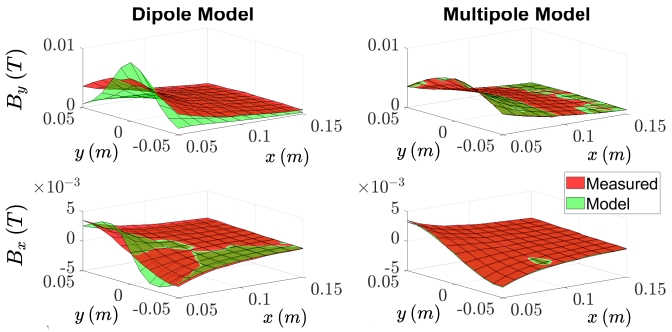


**Fig. 3:** Surface plots of the x- and y-components of the magnetic field ($B_x$ and $B_y$) obtained from measurements (red) and model (green) of the magnetic fields on a grid in the $xy$-plane in front of of an air-cored electromagnet of BigMag, comparing a least-squares fit of the point dipole model (left column, $P = 1$) to our multipole field model (right column, $P = 6$).

where $k > 0$ to exclude the monopole term, $P \in \mathbb{N}$ denotes the number of poles in the multipole expansion, and $a_k$ are unknown coefficients. The derivation of Eqn. 4 has been omitted for brevity.

The unknown coefficients ($a_k$) are obtained by measurement-informed linear least squares. The measurement setup, measurement equipment specifications, and measurements are described in, and taken from, [12]. Measurements ($\boldsymbol{B}(\boldsymbol{p}_{ij}, I_f)$) were performed at locations ($\boldsymbol{p}_{ij} = [x_i, y_j, 0]^T$) in a grid in front of the electromagnet, where $i = 1, 2, \ldots, m$ and $j = 1, 2, \ldots, n$, at a fitting current ($I_f = 4A$). The scalar coefficients ($a_k$) are subsequently computed from

$$\begin{bmatrix} \nabla\Psi_1(\boldsymbol{p}_{11}) & \ldots & \nabla\Psi_P(\boldsymbol{p}_{11}) \\ & \vdots & \\ \nabla\Psi_1(\boldsymbol{p}_{mn}) & \ldots & \nabla\Psi_P(\boldsymbol{p}_{mn}) \end{bmatrix}^\dagger \begin{bmatrix} \boldsymbol{B}(\boldsymbol{p}_{11}, I_f) \\ \vdots \\ \boldsymbol{B}(\boldsymbol{p}_{mn}, I_f) \end{bmatrix} = \begin{bmatrix} a_1 \\ \vdots \\ a_P \end{bmatrix}, \tag{5}$$

where $[\cdot]^\dagger$ denotes the Moore-Penrose pseudoinverse. The unit-current field and gradient map are thereafter given by

$$\boldsymbol{\beta}(\boldsymbol{p}) = \frac{\nabla\Psi(\boldsymbol{p})}{I_f}, \quad \boldsymbol{\beta}_\nabla(\boldsymbol{p}) = \begin{bmatrix} \frac{\partial\boldsymbol{\beta}(\boldsymbol{p})}{\partial x} & \frac{\partial\boldsymbol{\beta}(\boldsymbol{p})}{\partial y} & \frac{\partial\boldsymbol{\beta}(\boldsymbol{p})}{\partial z} \end{bmatrix}. \tag{6}$$

The above described fitting procedure is applied to the six mobile electromagnets inside BigMag (the actuation system utilized in this paper) such that the magnetic field within the workspace can be accurately computed given the electromagnet currents and positions.

A visual comparison between a linear least squares (LLSQ) fit of a point dipole model and the multipole model, for an air-cored electromagnet of BigMag, is given in Fig. 3. The norm of the root-mean-square error for the dipole fit is 1.18 mT, and for the multipole model 0.16 mT, for measurements with a resolution of 0.1 mT.

## III. Orientation Control

In this section we present the control scheme used for multi-point orientation control of a discretely magnetized continuum manipulator. Consider the experimental setup represented by

Fig. 1. The CM is suspended horizontally within the workspace, visualized using a stereo vision setup [21], and actuated with a magnetic field generated by $N_I \in \mathbb{R}^+$ electromagnets with currents $\left(\boldsymbol{I} \in \mathbb{R}^{N_I}\right)$ and $N_\theta \in \mathbb{R}^+$ pose parameters $\left(\boldsymbol{\theta} \in \mathbb{R}^{N_\theta}\right)$ (Fig. 5) [12]. First we measure the CM magnet poses with stereo vision. Second, the measured poses and actuation parameters $\{\boldsymbol{I}, \boldsymbol{\theta}\}$ are used to compute magnetic wrenches acting on the CM. Third, an orientation Jacobian is computed that maps incremental changes in $\{\boldsymbol{I}, \boldsymbol{\theta}\}$ to changes in CM magnet orientations. Finally, the CM magnets are steered towards a desired orientation by updating the actuation parameters $\{\boldsymbol{I}, \boldsymbol{\theta}\}$.

The control scheme (Fig. 4) is divided into four blocks (A-D), which are discussed in the subsections below. Axis-angle and quaternion representations for CM magnet orientations are used interchangeably.

### A. Magnet Pose Sensing

The stereo vision setup and shape reconstruction algorithm records the CM as a 3D point cloud and fits a 3D polynomial $(\boldsymbol{P}(s))$ from the CM proximal base to the distal tip (Fig. 1) [21]. From $\boldsymbol{P}(s)$ we obtain measured magnet positions $\left(\boldsymbol{p}_m \in \mathbb{R}^3\right)$ and orientations $(\boldsymbol{q}_m \in \mathbb{H})$, with knowledge of the magnet centerline positions $(s_m \in [0, L])$, as follows

$$\begin{aligned} &\boldsymbol{p}_m = \boldsymbol{P}(s_m), \quad \boldsymbol{p}'_m = \left(\boldsymbol{P}(s_m + \delta s) - \boldsymbol{P}(s_m)\right)/\delta s \\ &\phi_m = \cos^{-1}\left(\hat{\boldsymbol{z}} \cdot \hat{\boldsymbol{p}}'_m\right), \\ &\boldsymbol{k}_m = [\widehat{\hat{\boldsymbol{z}} \times \hat{\boldsymbol{p}}'_m}] \end{aligned} \Rightarrow \boldsymbol{q}_m = \begin{bmatrix} \cos\left(\frac{\phi_m}{2}\right) \\ \boldsymbol{k}_m \sin\left(\frac{\phi_m}{2}\right) \end{bmatrix}, \tag{7}$$

where $\hat{\boldsymbol{z}}$ is the unit global vertical axis superimposed on the magnet center of mass used as a reference for the CM magnet angle of rotation $(\phi_m \in \mathbb{R})$ and axis of rotation $\left(\boldsymbol{k}_m \in \mathbb{R}^3\right)$ (Fig. 5), and $\boldsymbol{p}'_m$ is the axial direction of the CM at magnet $m$. The inherent sign ambiguity of the axis-angle representation is solved by choosing the $\boldsymbol{k}_m$ of least angular distance from an arbitrary desired axis of rotation $\left(\boldsymbol{k}^d_m\right)$. The magnetic dipole moments $\left(\boldsymbol{\mu}_m \in \mathbb{R}^3\right)$ are known relative to, and therefore found from, $\boldsymbol{q}_m$ (Fig. 5).

### B. Magnetic Wrench

The magnetic wrench $\left(\boldsymbol{w}_m \in \mathbb{R}^6\right)$ exerted on $M \in \mathbb{N}$ CM magnets $(m = 1, \ldots, M)$ is computed from knowledge of the actuation parameters $\{\boldsymbol{I}, \boldsymbol{\theta}\}$ and magnet poses $\{\boldsymbol{p}_m, \boldsymbol{q}_m\}$. We compute a current-to-wrench map $(\boldsymbol{T})$, which is composed of a current-to-field map $\left(\boldsymbol{T}_\beta(\boldsymbol{p}_m, \boldsymbol{\theta}) : \mathbb{R}^{N_I} \to \mathbb{R}^{8M}\right)$ and field-to-wrench map $\left(\boldsymbol{T}_\mu(\boldsymbol{q}_m) : \mathbb{R}^{8M} \to \mathbb{R}^{6M}\right)$, defined at the center of mass of the magnets.

To compute $\boldsymbol{T}_\beta(\boldsymbol{p}_m, \boldsymbol{\theta})$, we first map the unit-current field map of each electromagnet (section II-B) to a global representation. Let $\{\mathcal{G}\}$ and $\{\mathcal{C}_j\}$ represent the global reference frame and body frame of an electromagnetic coil $(j = 1, \ldots, N_I)$, such that

$$\begin{aligned} {}^{\mathcal{G}}_{\mathcal{C}_j}\boldsymbol{\beta}(\boldsymbol{p}_m, \boldsymbol{\theta}) &= {}^{\mathcal{G}}_{\mathcal{C}_j}R(\boldsymbol{\theta})\, {}^{\mathcal{C}_j}\boldsymbol{\beta}\left({}^{\mathcal{C}_j}\boldsymbol{p}_m\right), \\ {}^{\mathcal{G}}_{\mathcal{C}_j}\boldsymbol{\beta}_\nabla(\boldsymbol{p}_m, \boldsymbol{\theta}) &= {}^{\mathcal{G}}_{\mathcal{C}_j}R(\boldsymbol{\theta})\, {}^{\mathcal{C}_j}\boldsymbol{\beta}_\nabla\left({}^{\mathcal{C}_j}\boldsymbol{p}_m\right) {}^{\mathcal{G}}_{\mathcal{C}_j}R(\boldsymbol{\theta})^T. \end{aligned} \tag{8}$$

In addition, we define a map $\mathbb{G}(\boldsymbol{\beta}_\nabla) : \mathbb{R}^{3\times3} \to \mathbb{R}^5$ that returns a vector of the five linearly independent spatial gradient components of the field [11]. The current-to-field map for a single CM magnet at position $\boldsymbol{p}_m$ is subsequently defined as

$$\boldsymbol{T}_\beta(\boldsymbol{p}_m, \boldsymbol{\theta}) = \begin{bmatrix} {}^{\mathcal{G}}_{\mathcal{C}_1}\boldsymbol{\beta} & \cdots & {}^{\mathcal{G}}_{\mathcal{C}_{N_I}}\boldsymbol{\beta} \\ \mathbb{G}\left({}^{\mathcal{G}}_{\mathcal{C}_1}\boldsymbol{\beta}_\nabla\right) & \cdots & \mathbb{G}\left({}^{\mathcal{G}}_{\mathcal{C}_{N_I}}\boldsymbol{\beta}_\nabla\right) \end{bmatrix}. \tag{9}$$

To compute $\boldsymbol{T}_\mu(\boldsymbol{q}_m)$, first consider the expression for the magnetic wrench $(\boldsymbol{w}_m)$ on a magnetic dipole within an external magnetic field,

$$\boldsymbol{w}_m = \begin{bmatrix} \boldsymbol{\tau}_m \\ \boldsymbol{f}_m \end{bmatrix} = \begin{bmatrix} \boldsymbol{\mu}_m(\boldsymbol{q}_m) \times \boldsymbol{B}(\boldsymbol{p}_m, \boldsymbol{I}, \boldsymbol{\theta}) \\ \nabla\big(\boldsymbol{\mu}_m(\boldsymbol{q}_m) \cdot \boldsymbol{B}(\boldsymbol{p}_m, \boldsymbol{I}, \boldsymbol{\theta})\big) \end{bmatrix}. \tag{10}$$

The above expression for the wrench is written to a matrix-vector multiplication with the field-to-wrench map,

$$\boldsymbol{T}_\mu(\boldsymbol{q}_m) = \begin{bmatrix} \big[\boldsymbol{\mu}_m(\boldsymbol{q}_m)\big]_\times & 0 \\ 0 & \mathbb{M}\big(\boldsymbol{\mu}_m(\boldsymbol{q}_m)\big) \end{bmatrix}, \tag{11}$$

where $[\cdot]_\times : \mathbb{R}^3 \to \mathbb{R}^{3\times3}$ represents a map to a skew-symmetric matrix, and $\mathbb{M}(\boldsymbol{\mu}) : \mathbb{R}^3 \to \mathbb{R}^{3\times5}$ maps the independent spatial field gradients to forces on the dipole [11],

$$\mathbb{M}(\boldsymbol{\mu}) = \begin{bmatrix} \mu_x & \mu_y & \mu_z & 0 & 0 \\ 0 & \mu_x & 0 & \mu_y & \mu_z \\ -\mu_z & 0 & \mu_x & -\mu_z & \mu_y \end{bmatrix}. \tag{12}$$

The current-to-field and field-to-wrench maps can then be multiplied to map currents $(\boldsymbol{I})$ in the system to magnetic wrenches on the CM magnets,

$$\begin{aligned} \boldsymbol{w}_m &= \boldsymbol{T}_\mu(\boldsymbol{q}_m)\boldsymbol{T}_\beta(\boldsymbol{p}_m, \boldsymbol{\theta})\boldsymbol{I} \\ &= \boldsymbol{T}(\boldsymbol{p}_m, \boldsymbol{q}_m, \boldsymbol{\theta})\boldsymbol{I}. \end{aligned} \tag{13}$$

For $M$ CM magnets $(m = 1, \ldots, M)$, we then obtain a vector of wrenches $\left(\boldsymbol{w} = [\boldsymbol{w}_1^T, \boldsymbol{w}_2^T, \ldots, \boldsymbol{w}_M^T]^T\right)$. Given the magnetic wrenches on the magnets, we can solve the CM statics as a boundary value problem (BVP) and obtain the theoretical shape (Eqn. 2). This shape solution contains the theoretical magnet poses $\{{}^t\boldsymbol{p}_m, {}^t\boldsymbol{q}_m\}$, which are required to compute the orientation Jacobian.

### C. Orientation Jacobian

The orientation Jacobian maps incremental changes in actuation parameters to changes in magnet orientations. Let $N_A = N_I + N_\theta$ represent the number of actuation parameters. Then the orientation Jacobian $\left(\boldsymbol{J}_{k\phi} \in \mathbb{R}^{2M\times N_A}\right)$ is numerically computed by solving $N_A$ BVPs (section II-A), each concerning a virtually incremented actuation parameter, a resulting new virtual wrench on the CM, and a following virtual manipulator response predicted from the Cosserat rod model. An informed guess for the optimization vector $\left(\boldsymbol{\xi}^i\right)$ is provided before solving each BVP (Fig. 2).

Algorithm 1 presents the procedure of computing $\boldsymbol{J}_{k\phi}$, where we simulate open loop control cycles. First, one actuation

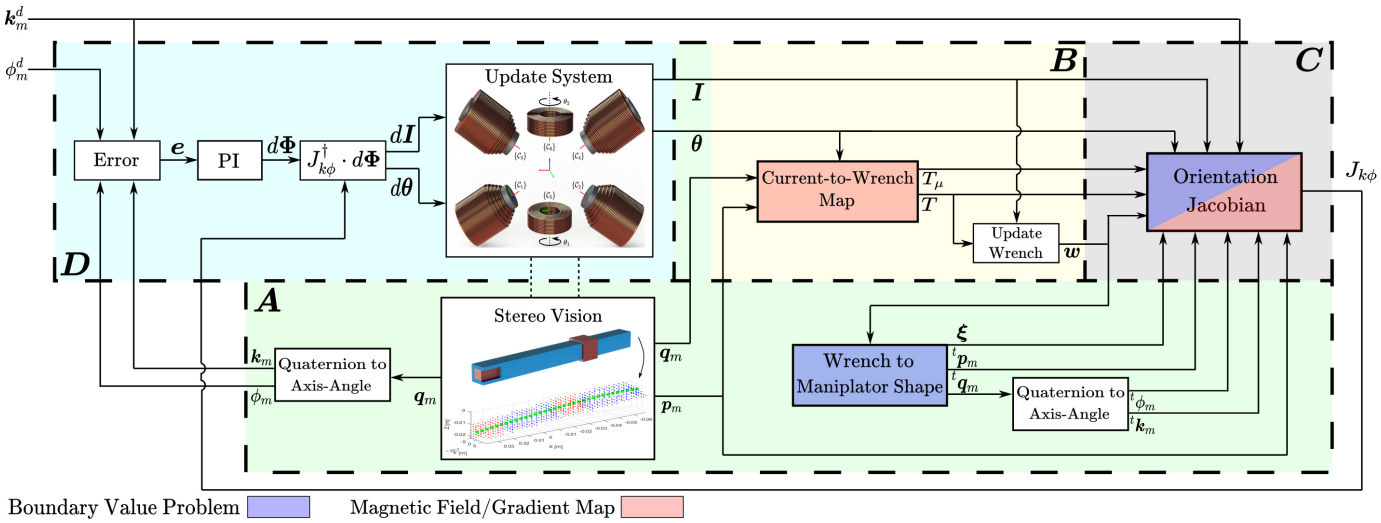


**Fig. 4:** Orientation control diagram. $(\boldsymbol{A})$ A stereo vision setup records a 3D point cloud of the continuum manipulator (CM) that holds information about the measured magnet poses $\{\boldsymbol{p}_m, \boldsymbol{q}_m\}$. Knowledge of the magnetic wrench $(\boldsymbol{w})$ acting on the magnets is used to solve the CM statics (shape) with a Cosserat rod model, which holds information about theoretical magnet poses $\{{}^t\boldsymbol{p}_m, {}^t\boldsymbol{q}_m\}$. $(\boldsymbol{B})$ Measured magnet poses and electromagnet currents and positions $\{\boldsymbol{I}, \boldsymbol{\theta}\}$ of the system are used to compute the magnetic wrench. $(\boldsymbol{C})$ An orientation Jacobian $(\boldsymbol{J}_{k\phi})$ is computed (algorithm 1) that maps incremental changes in $\{\boldsymbol{I}, \boldsymbol{\theta}\}$ to changes in magnet orientations. $(\boldsymbol{D})$ The orientation Jacobian and error between desired and measured magnet orientation are used to update $\{\boldsymbol{I}, \boldsymbol{\theta}\}$.

parameter is incremented and the change in exerted magnetc wrench $(d\boldsymbol{w})$ computed. Third, an informed guess, given by

$$\boldsymbol{\xi}^i\left(\boldsymbol{\xi}, d\boldsymbol{w}, \boldsymbol{p}_m\right) = \boldsymbol{\xi} + \sum_{m=1}^{M} \begin{bmatrix} d\boldsymbol{f}_m \\ d\boldsymbol{\tau}_m + (\boldsymbol{p}_m - \boldsymbol{p}_0) \times d\boldsymbol{f}_m \end{bmatrix}, \quad (14)$$

is formulated as an initial solution to the BVP, with $\boldsymbol{p}_0$ the CM base position (Fig. 2). The CM statics are subsequently solved as a BVP to obtain the shape solution $\left(\boldsymbol{Y}(\boldsymbol{\xi}^i)\right)$. Fourth, the new theoretical magnet poses $\{{}^t\bar{\boldsymbol{k}}_m, {}^t\bar{\phi}_m\}$ are taken from the shape solution. Finally, the linear approximation of the change in CM magnet orientation due to a change in electromagnet current $(dI_j,\ j = 1, \ldots, N_I)$ is defined as

$$\begin{aligned} \frac{d\left(\boldsymbol{k}_m^d \cdot \boldsymbol{k}_m\right)}{dI_j} &= \frac{\boldsymbol{k}_m^d \cdot \left({}^t\bar{\boldsymbol{k}}_m - {}^t\boldsymbol{k}_m\right)}{dI_j}, \\ \frac{d\phi_m}{dI_j} &= \frac{{}^t\bar{\phi}_m - {}^t\phi_m}{dI_j}, \end{aligned} \quad (15)$$

and similarly for a change in electromagnet pose $(d\theta_l,\ l = 1, \ldots, N_\theta)$; $\boldsymbol{k}_m^d$ denotes the desired axis of rotation of the CM magnet. The steps are repeated for all $N_A$ actuation parameters. The orientation Jacobian is then, for $M = 2$ CM magnets (Fig. 5), constructed as

$$\boldsymbol{J}_{k\phi} = \begin{bmatrix} \frac{d\left(\boldsymbol{k}_1^d \cdot \boldsymbol{k}_1\right)}{dI_1} & \cdots & \frac{d\left(\boldsymbol{k}_1^d \cdot \boldsymbol{k}_1\right)}{dI_{N_I}} & \frac{d\left(\boldsymbol{k}_1^d \cdot \boldsymbol{k}_1\right)}{d\theta_1} & \cdots \\ \frac{d\phi_1}{dI_1} & \cdots & \frac{d\phi_1}{dI_{N_I}} & \frac{d\phi_1}{d\theta_1} & \cdots \\ \frac{d\left(\boldsymbol{k}_2^d \cdot \boldsymbol{k}_2\right)}{dI_1} & \cdots & \frac{d\left(\boldsymbol{k}_2^d \cdot \boldsymbol{k}_2\right)}{dI_{N_I}} & \frac{d\left(\boldsymbol{k}_2^d \cdot \boldsymbol{k}_2\right)}{d\theta_1} & \cdots \\ \frac{d\phi_2}{dI_1} & \cdots & \frac{d\phi_2}{dI_{N_I}} & \frac{d\phi_2}{d\theta_1} & \cdots \end{bmatrix}. \quad (16)$$

The orientation Jacobian $(\boldsymbol{J}_{k\phi})$ represents a linear map from increments in actuation parameters to changes in magnet orientation, and is used to update the actuation parameters.

### D. Updating Actuation Parameters

The actuation parameters $\{\boldsymbol{I}, \boldsymbol{\theta}\}$ are updated to decrease the error $(\boldsymbol{e}_m)$ between given desired magnet orientation $\{\boldsymbol{k}_m^d, \phi_m^d\}$ and measured orientation $\{\boldsymbol{k}_m, \phi_m\}$, which is computed as

$$\boldsymbol{e}_m = \begin{bmatrix} 1 - \boldsymbol{k}_m^d \cdot \boldsymbol{k}_m \\ \phi_m^d - \phi_m \end{bmatrix} \Rightarrow \boldsymbol{e} = \begin{bmatrix} \boldsymbol{e}_1 \\ \boldsymbol{e}_2 \end{bmatrix}. \quad (17)$$

The error $(\boldsymbol{e})$ is given to a proportional-integral controller to compute an orientation step $(d\boldsymbol{\Phi})$. Then the actuation parameters are updated according to

$$\begin{bmatrix} d\boldsymbol{I}^T, & d\boldsymbol{\theta}^T \end{bmatrix}^T = \boldsymbol{J}_{k\phi}^{\dagger} \cdot d\boldsymbol{\Phi}, \quad (18)$$

The Moore-Penrose pseudoinverse of $\boldsymbol{J}_{k\phi}$ is computed through singular value decomposition as $\boldsymbol{J}_{k\phi}^{\dagger} = VS^{\dagger}U^T$, where $S$ is a diagonal matrix of singular values $(\sigma_i > \sigma_{i+1})$. To improve numerical stability we select singular values according to

$$S_{ii} = \begin{cases} \sigma_i & \text{If } \sigma_1/\sigma_i \leq 10^5 \\ 0 & \text{If } \sigma_1/\sigma_i > 10^5 \end{cases}. \quad (19)$$

## IV. Experiments and Simulation

The experiments and simulations in this section aim to show that it is possible to achieve convergence of multiple magnets to desired orientations by generating a non-homogeneous magnetic field. First, experimental validation of planar steering is described, followed by simulated results of 3D steering. The actuation of the CM, in the experiment and simulation, can be seen in the supplementary video.

**Algorithm 1:** Computation of the Orientation Jacobian

**Input :** · Magnet pose info $\boldsymbol{p}_m, {}^t\boldsymbol{p}_m, \{{}^t\boldsymbol{k}_m, {}^t\phi_m\}$
· Cosserat model base state parameters $\boldsymbol{\xi}$
· Current- and Field-to-Wrench maps $\boldsymbol{T}, \boldsymbol{T}_\mu$
· Magnetic wrench $\boldsymbol{w}$
· Actuation parameters $\boldsymbol{I}, \boldsymbol{\theta}$
· Desired magnet axes of rotation $\boldsymbol{k}_m^d$

**Output :** Orientation Jacobian, $\boldsymbol{J}_{k\phi}$

$dI, d\theta \in \mathbb{R}^+$
/* Current to Orientation Change */
**for** $j \leftarrow 1$ **to** $N_I$ **do**
  $\boldsymbol{I}_j = \boldsymbol{I}_j + dI$
  $\bar{\boldsymbol{w}} = \boldsymbol{T}\boldsymbol{I}$ // New wrench
  $d\boldsymbol{w} = \bar{\boldsymbol{w}} - \boldsymbol{w}$ // Change in wrench
  Compute informed guess $\boldsymbol{\xi}^i(\boldsymbol{\xi}, d\boldsymbol{w}, \boldsymbol{p}_m)$
  Solve manipulator shape $\boldsymbol{Y}(\bar{\boldsymbol{w}}, \boldsymbol{\xi}^i)$ // BVP (2)
  Get new magnet poses $\{{}^t\bar{\boldsymbol{p}}_m, {}^t\bar{\boldsymbol{k}}_m, {}^t\bar{\phi}_m\} \leftarrow \boldsymbol{Y}$
  Fill column of $\boldsymbol{J}_{k\phi}$
  $\boldsymbol{I}_j = \boldsymbol{I}_j - dI$
**end for**
/* Position to Orientation Change */
**for** $l \leftarrow 1$ **to** $N_\theta$ **do**
  $\boldsymbol{\theta}_l = \boldsymbol{\theta}_l + d\theta$
  Recompute $\boldsymbol{T}_\beta(\boldsymbol{p}_m, \boldsymbol{\theta})$ and $\boldsymbol{T} = \boldsymbol{T}_\mu \boldsymbol{T}_\beta$ // (9)
  $\bar{\boldsymbol{w}} = T\boldsymbol{I}$ // New wrench
  ⋮
  $\boldsymbol{\theta}_l = \boldsymbol{\theta}_l - d\theta$
**end for**
**return** $\boldsymbol{J}_{k\phi}$

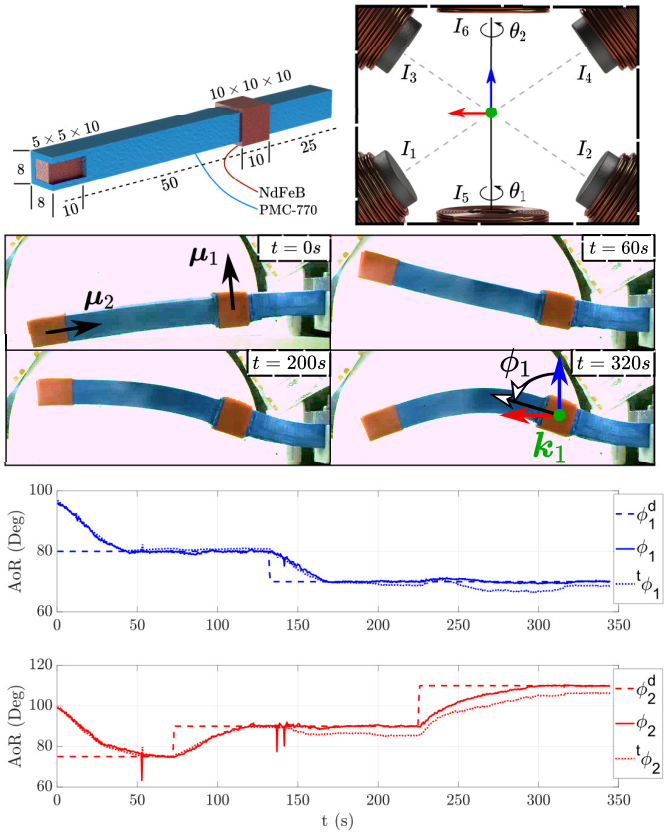


**Fig. 5:** Model of the continuum manipulator (CM) consisting of flexible polyurethane rubber (PMC-770) and rigid neodymium magnets (NdFeB), with dimensions given in millimeters. The magnet dipole moments, $\boldsymbol{\mu}_m$, are shown at $t = 0$s. Magnet angles of rotation (AoR) are measured relative to the global $\hat{\boldsymbol{z}}$ axis, superimposed on the magnet center, shown at $t = 320$s. The CM is actuated inside the workspace of BigMag in plane with six electromagnets [12]. Side views of time-evolved shapes of the continuum manipulator are shown and desired, $\phi_m^d$, measured $\phi_m$, and predicted, ${}^t\phi_m$, AoR are plot for magnet 1 (blue) and 2 (red) in degrees against time $t$.

### A. Experiment

The experimental setup is represented by Fig. 1. The CM consists of subsections of flexible polyurethane rubber (PMC-770, Smooth-On Inc., USA) and rigid neodymium (NdFeb) magnets. Dipole moments $(\boldsymbol{\mu}_m)$ and dimensions are shown in Fig. 5. The magnetic actuation system, BigMag, consists of six electromagnets oriented towards the center of a spherical workspace of diameter 11cm (Fig. 5, $N_I = 6$, $N_\theta = 2$). The workspace is recorded using two Dalsa Genie Nano RGB cameras (Teledyne Dalsa, Waterloo, ON, Canada). The control system is implemented in C++14 on a computer running a Linux Ubuntu 14.04.01 OS with an Intel Xeon E5 CPU, NVidia Quadro K4200 GPU, and 32 GB RAM [21].

Experiments were performed in 2D where the CM is suspended in plane with the actuator electromagnets $\left(\boldsymbol{k}_m^d = \boldsymbol{k}_m = \hat{\boldsymbol{y}}\right)$. Fig. 5 provides side views of time-evolved shapes of the CM during the experiment. The measured magnet angles of rotation (AoR, $\phi_m$) are defined relative to the global $\hat{\boldsymbol{z}}$ ($t = 320$s). Steps in AoR are provided manually during the experiment, keeping electromagnet currents within the limits of $\pm 8$A. The AoR are shown against the elapsed time.

The step size in current $(dI)$ and position $(d\theta)$ to compute the orientation Jacobian $(\boldsymbol{J}_{k\phi})$ were determined as 0.2A and 2°, respectively, based on trial and error. The computation time for $\boldsymbol{J}_{k\phi}$ was $158 \pm 64$ms and $165 \pm 53$ms with and without the informed guess (Eqn. 14), respectively.

### B. Simulation

Fig. 6 shows side, top, and isometric views of the CM's shape during simulation with iteration number i $\in \mathbb{N}$. The magnetic field is generated with a virtual clone of BigMag extended with additional electromagnets ($N_I = 14$, $N_\theta = 2$). A unique non-homogeneous field is generated at the center of mass of each magnet to simultaneously steer the theoretical AoR $({}^t\phi_m)$ of the magnets to their respective target AoR $\left(\phi_m^d\right)$. In addition, the theoretical axes of rotation $({}^t\boldsymbol{k}_m)$ of the magnets are steered towards their respective target $\left(\boldsymbol{k}_m^d\right)$ to minimize the angular distance ($\angle$Axis) between them. The computation time required to compute the orientation Jacobian with and without providing an informed guess is $260 \pm 41$ ms and $420 \pm 16$, respectively.

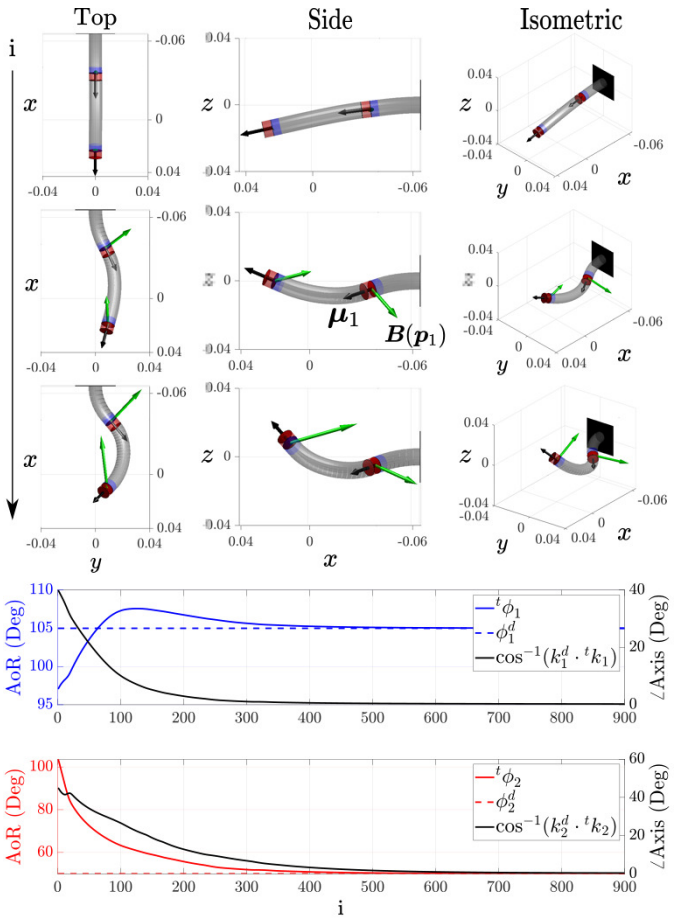


**Fig. 6:** Top, side, and isometric views of CM shapes at starting, intermediate, and final iteration numbers (i) with dimensions shown in meters. Trajectories of the theoretical magnet angles of rotation (AoR, ${}^t\phi_m$), for the proximal and distal magnet, are given in blue and red, respectively. Also, the trajectories of the angular distances between the theoretical and desired axes of rotation ($\angle$Axis) are shown.

## V. Discussion

The closed-loop response of the magnet orientations (Fig. 5) shows the control algorithm can achieve accurate independent multi-point orientation control in 2D. Compared to other works, the magnetic forces cannot be ignored due to the non-homogeneity of the actuation field and the close proximity of the magnets; Fig. 7 shows the deflection of the CM for the experiment in Sec. IV-A calculated with the Cosserat rod model, both with and without magnetic forces. It is noticeable that the calculated shape of the manipulator when the magnetic forces are ignored is significantly different from when they are included. Additionally, it was also necessary to formulate and apply an accurate magnetic field model to the electromagnets in BigMag, and use a Cosserat rod model to simulate movement of the CM in a non-homogeneous magnetic field. The accuracy of the models determine the accuracy of the terms in the orientation Jacobian used for control.

The experiments that showed independent orientation control of two magnets were limited to 2D because of the available actuation DOFs. The minimum bounds on the necessary magnetic DOFs is three per magnet for orientation control, considering magnetic forces negligible. However, because the effect of forces is pronounced for magnets in close proximity, more than three magnetic actuation DOFs per magnet are required. Since the magnetic forces are dependent on five field gradient terms, the maximum additional actuation DOFs per magnet is five. Thus, for singularity-free wrench control a total of eight magnetic DOFs per magnet are required, as proven by Petruska and Nelson [9]. Therefore we limited our experiments to the planar case and performed a 3D simulation with the maximum bound of sixteen DOFs for two magnets. In practice fewer may be required since the solution of the magnetic wrench is not unique. Furthermore, such large multi-coil systems have a limited workspace and are infeasible in practice. These systems are would ideally be replaced by a system with dedicated (electro)magnets for each CM magnet, attached as end-effectors to multi-DOF robot arms [13]. In this case the terms in the orientation Jacobian ($\boldsymbol{J}_{k\phi}$) would be replaced according to the available DOFs: (electro)magnet poses and currents. In addition, with an application-specific acutation system, it would be possible to utilize the null-space of $\boldsymbol{J}_{k\phi}$ to accomplish a secondary task, such as increasing the static equilibrium stability of the CM [20].

The time required for CM shape reconstruction and computing $\boldsymbol{J}_{k\phi}$ (approximately the same) limited the achievable control frequency to 2Hz, which is less than desired for closed-loop control. Full shape reconstruction of a CM is in practice infeasible with stereo vision or ultrasound due to time constraints and because torsion cannot be reliably measured. For this reason, other sensing modalities such as fiber Bragg gratings should be considered [27]. Furthermore, the computational efficiency for constructing $\boldsymbol{J}_{k\phi}$ can be significantly improved because the necessary (independent) boundary value problems (BVPs) were solved in series rather than in parallel. With parallel computing the necessary computation time could be reduced to that of a single constituent BVP, which took on average 20ms. With the improved guess (Eqn. 14) we did not observe an increase in control frequency during closed-loop experiments, whereas in open-loop simulation the informed guess improved the computation time. This is because both the feedback and the forward model are calculated using the Cosserat rod model. However, when stereo vision is used for closed-loop control, the CM shape feedback diverges from the forward model.

Finally, the formulated magnetic field (gradient) model has shown able to accurately describe the generated magnetic field of an azimuthally symmetric field source. Because the model conforms to Maxwell's equations for fields in a current-free workspace, it can also be applied to accurately estimate the spatial gradients of the field. Compared to previous works, this provides the ability to utilize magnetically exerted forces in addition to torques for closed-loop control of magnetized CMs.

## VI. Conclusions and Future Work

In this paper, an approach for closed-loop multi-point orientation control of discretely magnetized CMs is presented. The effect of magnetic forces must be considered and the novel magnetic field model was able to accurately describe the

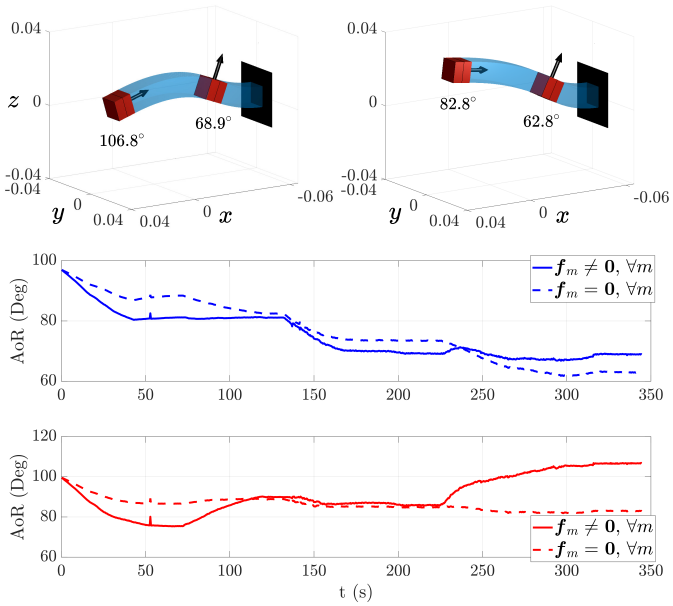


**Fig. 7:** A comparison between the theoretical shape of the CM, including and excluding magnetic forces ($\boldsymbol{f}_m$). At the top is the shape of the CM with (left) and without (right) magnetic forces at $t = 320s$ in Fig. 5; dimensions are shown in meters. The trajectories of the theoretical angles of rotation (AoR, ${}^t\phi_m$) for the proximal and distal magnet are shown in blue and red, respectively.

magnetic field and field gradients required for computing the exerted magnetic torques and forces. In addition, the employed quasi-static Cosserat rod model of the CM was able to predict the magnet orientation changes in a varying non-homogeneous magnetic field. Both the field and Cosserat rod models were applied to construct a numerically-computed orientation Jacobian to linearize changes in actuation parameters to changes in magnet orientations. In the end, the presented control strategy has shown able to achieve accurate independent orientation control of two permanent magnets in 2D inside BigMag, and in 3D simulation using an extended virtual clone of BigMag. However, the computational cost of shape reconstruction and the Jacobian limited the control frequency to 2Hz.

Future work will focus on implementing parallel computing and we hypothesize that this will lead to a significant increase in the achievable control frequency. Futhermore, since the presented magnetic field map is accurate in describing the spatial gradients of the magnetic field, we would like to apply it to magnetic force-based manipulation tasks.

## References


[1] J. Burgner-Kahrs, D. C. Rucker, and H. Choset, "Continuum robots for medical applications: A survey," *IEEE Transactions on Robotics*, vol. 31, no. 6, pp. 1261–1280, 2015.

[2] T. da Veiga, J. H. Chandler, P. Lloyd, G. Pittiglio, N. J. Wilkinson, A. K. Hoshiar, R. A. Harris, and P. Valdastri, "Challenges of continuum robots in clinical context: a review.," *Progress in Biomedical Engineering*, 2020.

[3] T. L. Thomas, V. K. Venkiteswaran, G. Ananthasuresh, and S. Misra, "A monolithic compliant continuum manipulator: A proof-of-concept study," *Journal of Mechanisms and Robotics*, vol. 12, no. 6, 2020.

[4] J. Sikorski, S. Mohanty, and S. Misra, "Milimac: Flexible catheter with miniaturized electromagnets as a small-footprint system for microrobotic tasks," *IEEE Robotics and Automation Letters*, vol. 5, no. 4, pp. 5260–5267, 2020.

[5] G. Pittiglio, L. Barducci, J. W. Martin, J. C. Norton, C. A. Avizzano, K. L. Obstein, and P. Valdastri, "Magnetic levitation for soft-tethered capsule colonoscopy actuated with a single permanent magnet: a dynamic control approach," *IEEE Robotics and Automation Letters*, vol. 4, no. 2, pp. 1224–1231, 2019.

[6] Y. Kim, G. A. Parada, S. Liu, and X. Zhao, "Ferromagnetic soft continuum robots," *Sci. Robot*, vol. 4, no. 33, p. 7329, 2019.

[7] P. Lloyd, A. K. Hoshiar, T. da Veiga, A. Attanasio, N. Marahrens, J. H. Chandler, and P. Valdastri, "A learnt approach for the design of magnetically actuated shape forming soft tentacle robots," *IEEE Robotics and Automation Letters*, vol. 5, no. 3, pp. 3937–3944, 2020.

[8] G. Z. Lum, Z. Ye, X. Dong, H. Marvi, O. Erin, W. Hu, and M. Sitti, "Shape-programmable magnetic soft matter," *Proceedings of the National Academy of Sciences*, vol. 113, no. 41, pp. E6007–E6015, 2016.

[9] A. J. Petruska and B. J. Nelson, "Minimum bounds on the number of electromagnets required for remote magnetic manipulation," *IEEE Transactions on Robotics*, vol. 31, no. 3, pp. 714–722, 2015.

[10] M. P. Kummer, J. J. Abbott, B. E. Kratochvil, R. Borer, A. Sengul, and B. J. Nelson, "Octomag: An electromagnetic system for 5-dof wireless micromanipulation," *IEEE Transactions on Robotics*, vol. 26, no. 6, pp. 1006–1017, 2010.

[11] S. Salmanipour and E. Diller, "Eight-degrees-of-freedom remote actuation of small magnetic mechanisms," *IEEE International Conference on Robotics and Automation (ICRA)*, 2018.

[12] J. Sikorski, I. Dawson, A. Denasi, E. E. Hekman, and S. Misra, "Introducing bigmag—a novel system for 3d magnetic actuation of flexible surgical manipulators," pp. 3594–3599, 2017.

[13] J. Sikorski, C. M. Heunis, F. Franco, and S. Misra, "The armm system: An optimized mobile electromagnetic coil for non-linear actuation of flexible surgical instruments," *IEEE Transactions on Magnetics*, vol. 55, no. 9, pp. 1–9, 2019.

[14] C. M. Heunis, J. Sikorski, and S. Misra, "Flexible instruments for endovascular interventions: Improved magnetic steering, actuation, and image-guided surgical instruments," *IEEE Robotics & Automation Magazine*, vol. 25, no. 3, pp. 71–82, 2018.

[15] F. Ongaro, C. M. Heunis, and S. Misra, "Precise model-free spline-based approach for magnetic field mapping," *IEEE Magnetics Letters*, vol. 10, pp. 1–5, 2018.

[16] A. J. Petruska and J. J. Abbott, "Optimal permanent-magnet geometries for dipole field approximation," *IEEE Transactions on Magnetics*, vol. 49, no. 2, pp. 811–819, 2012.

[17] A. J. Petruska, J. Edelmann, and B. J. Nelson, "Model-based calibration for magnetic manipulation," *IEEE Transactions on Magnetics*, vol. 53, no. 7, pp. 1–6, 2017.

[18] V. K. Venkiteswaran, J. Sikorski, and S. Misra, "Shape and contact force estimation of continuum manipulators using pseudo rigid body models," *Mechanism and Machine theory*, vol. 139, pp. 34–45, 2019.

[19] D. C. Rucker and R. J. Webster III, "Statics and dynamics of continuum robots with general tendon routing and external loading," *IEEE Transactions on Robotics*, vol. 27, no. 6, pp. 1033–1044, 2011.

[20] J. Edelmann, A. J. Petruska, and B. J. Nelson, "Magnetic control of continuum devices," *The International Journal of Robotics Research*, vol. 36, no. 1, pp. 68–85, 2017.

[21] J. Sikorski, A. Denasi, G. Bucchi, S. Scheggi, and S. Misra, "Vision-based 3-d control of magnetically actuated catheter using bigmag—an array of mobile electromagnetic coils," *IEEE/ASME Transactions on Mechatronics*, vol. 24, no. 2, pp. 505–516, 2019.

[22] V. N. Le, N. H. Nguyen, K. Alameh, R. Weerasooriya, and P. Pratten, "Accurate modeling and positioning of a magnetically controlled catheter tip," *Medical Physics*, vol. 43, no. 2, pp. 650–663, 2016.

[23] S. Jeon, A. K. Hoshiar, K. Kim, S. Lee, E. Kim, S. Lee, J.-y. Kim, B. J. Nelson, H.-J. Cha, B.-J. Yi, *et al.*, "A magnetically controlled soft microrobot steering a guidewire in a three-dimensional phantom vascular network," *Soft Robotics*, vol. 6, no. 1, pp. 54–68, 2019.

[24] S. Antman, *Nonlinear Problems of Elasticity*. Springer-Verlag, 1995.

[25] J. Till, V. Aloi, and C. Rucker, "Real-time dynamics of soft and continuum robots based on cosserat rod models," *The International Journal of Robotics Research*, vol. 38, no. 6, pp. 723–746, 2019.

[26] D. J. Griffiths, *Introduction to electrodynamics*. Prentice Hall, 2005.

[27] F. Khan, A. Donder, S. Galvan, F. R. y Baena, and S. Misra, "Pose measurement of flexible medical instruments using fiber bragg gratings in multi-core fiber," *IEEE Sensors Journal*, vol. 20, no. 18, pp. 10955–10962, 2020.